



Contents lists available at ScienceDirect

International Journal of Solids and Structures

journal homepage: www.elsevier.com/locate/ijsostr

An extended hydrostatic–deviatoric strain energy density decomposition for phase-field fracture theories

Parnian Hesammokri^{*}, Haiyang Yu, Per Isaksson*Solid Mechanics, The Ångström Laboratory, Uppsala University, SE-751 21 Uppsala, Sweden*

ARTICLE INFO

Keywords:
Phase-field
Decomposition
Mixed-mode fracture

ABSTRACT

The interest in using phase-field theories to numerically analyze fracture has sky-rocketed in the last years. However, in phase-field fracture models are splits, or decompositions, of the strain energy density vital to avoid interpenetration of crack surfaces and to select physically trustworthy crack paths. The most popular decomposition strategies use either a spectral decomposition or a hydrostatic–deviatoric decomposition. Both decompositions have significant disadvantages; the most important is that none of them can handle mixed-mode load scenarios in compression. To circumvent these problems, a generalized decomposition method is derived that unifies some features of the hydrostatic–deviatoric and spectral decompositions, enhanced with a classical Mohr–Coulomb failure criterion. The derived decomposition scheme has the potential to judge whether or not a compressive deformation field will assist in the crack driving process in brittle materials. The enhanced decomposition is scrutinized in numerical models and revealing biaxially loaded crack experiments in global compression. Simulations using the decomposition scheme capture the experiments in a remarkable way: complex crack patterns are reproduced, as well as critical loads. The enhanced decomposition strategy hence provides mechanistic insight into fracture processes in brittle materials subject to mixed-mode loads.

1. Introduction

Why and how cracks spread in materials is of essential concern in numerous scientific disciplines and technological applications. Fracture is often analyzed numerically within a finite element context using either discrete or diffuse crack representations. Approaches using a discrete representation make use of strong discontinuities embedded at the intra-element level (Moës and Belytschko, 2002; Armero and Linder, 2009) and require additional criteria based on stresses, strains, or energy release rates, and special treatments such as virtual crack closure techniques and complicated remeshing techniques. In contrast, approaches using a diffuse crack representation (cf. Peerlings et al., 1996; Areias et al., 2016; Miehe et al., 2010b,a; Borden et al., 2012) retain the continuity of the displacement field, such as continuum damage models and phase-field fracture models. Perhaps the most attractive feature of phase-field fracture models is that the crack mechanics is inherently obtained from a minimization problem that couples the strain and fracture energies. This enables the treatment of complex crack scenarios such as crack initiation, growth, merging, and branching without any need for remeshing, which distinguish them in a remarkable way from traditional modeling techniques. Phase-field fracture models have quickly become popular, which is explained by their extreme versatility (e.g. dynamics Borden et al., 2012; Larsen et al., 2010; Hofacker and

Miehe, 2012; Carlsson and Isaksson, 2018, 2019; Schlüter et al., 2016, or heterogeneous materials Kuhn and Müller, 2016; Espadas-Escalante et al., 2019; Espadas-Escalante and Isaksson, 2019).

Phase-field fracture methods are based on a variational principle closely related to the variational principles suggested by Griffith in 1921, but originated much later, in the seminal work of Francfort and Marigo (1998), and later Bourdin et al. (2000). Decompositions, or splits, of the strain energy density into positive (tensile) and negative (compressive) parts are often used to avoid interpenetration of cracked surfaces and to select physically trustworthy crack paths. Using such decomposition method, the positive part of the strain energy density is assumed to assist in degrading the material while the negative part is assumed not to effect the degrading process. Today, the by far most common methods to decompose the strain energy density use either a hydrostatic–deviatoric decomposition (Amor et al., 2009) or a spectral decomposition (Miehe et al., 2010b). Although these methods sometimes show good agreement with experiments (cf. Cajuhi et al., 2018; Zhang et al., 2017; Santillán et al., 2017; Pham et al., 2017) they are generally not applicable to mixed-mode loading conditions. For instance, the spectral decomposition is limited in shear-dominated loadings, where the material stiffness may never be completely lost even

^{*} Corresponding author.

E-mail address: parnian.hesammokri@angstrom.uu.se (P. Hesammokri).

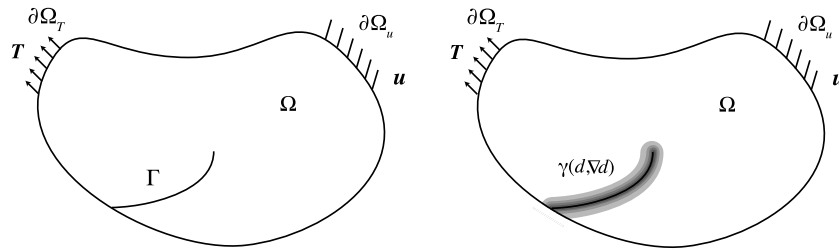


Fig. 1. Discrete vs diffusive crack representation.

though a fracture is fully developed. The hydrostatic–deviatoric decomposition is limited in mixed-mode compressive loading conditions since all the strain energy density associated with shape deformation may result in a complete stiffness loss even though the crack surfaces may come in contact (i.e. the material can carry load). These features considerably limit the capability of phase-field models to simulate fractures subject to shear and compressive loads.

In the literature, the application of shear or compression-dominated phase-field fractures is mainly related to rock mechanics. An attempt to modify the spectral decomposition for mixed-mode brittle fractures was proposed by Zhang et al. (2017), who assumed different fracture toughnesses (or critical energy release rates) in opening and shearing crack growth. Other similar modifications for mixed-mode fracture have been suggested, cf. Spetz et al. (2020, 2021). However, these modifications are not completely satisfactory, mainly because they are based on various spectral decomposition formulations preventing material stiffness degradation even when cracks are fully developed under pure shear load.

The aim of this study is to formulate a decomposition strategy that captures reliable fracture paths and material degradation in both compression and shear loading scenarios, thus overcoming the aforementioned challenges. The developed decomposition is scrutinized in numerical models and compared to biaxially loaded fracture experiments in global compression on brittle rock-like materials.

2. Theory

Consider an isotropic linearly-elastic body Ω (Fig. 1) with exterior $\partial\Omega$ and a discrete crack Γ . In this domain, $\partial\Omega_T$ is subject to traction T and $\partial\Omega_u$ is subject to displacement u . The total free energy of the system can be written as

$$\Pi(\mathbf{u}, d) = \int_{\Omega} \Psi_e d\Omega + \int_{\Gamma} G_c ds, \quad (1)$$

where Ψ_e is the strain energy density and G_c is critical energy release rate of the material. A damage parameter d is introduced ($0 \leq d \leq 1$) so that the material is intact when $d = 0$ and fully damaged when $d = 1$.

The last term in (1) represents the energy consumed by surface creation. In the phase-field implementation, the discrete crack Γ is represented by a crack density function $\gamma(d, \nabla d)$, Fig. 1. The crack density functional, typically chosen as either first order or second order in d , can be chosen with a great freedom from the family of elliptic functionals approximating the Mumford–Shah functional (Braides, 1998). Here, a crack density functional which is linear in d and quadratic in ∇d (Pham et al., 2011) is used, which has the benefit of having a distinct elastic limit. The second term in (1) can now be written as

$$\int_{\Gamma} G_c ds = G_c \int_{\Omega} \gamma(d, \nabla d) d\Omega, \quad (2)$$

$$\gamma(d, \nabla d) = \frac{3}{8l} (d + l^2 \nabla d \cdot \nabla d), \quad (3)$$

where l is a regularization parameter, controlling the width of the regularized crack. Further, to prevent crack growth under compression, the strain energy density is decomposed into a tensile/positive part

and a compressive/negative part, where only the positive part affects damage (stiffness degradation), cf. Ambati et al. (2015), i.e.,

$$\int_{\Omega} \Psi_e d\Omega = \int_{\Omega} [(1-d)^2 \Psi_e^+ + \Psi_e^-] d\Omega. \quad (4)$$

The Cauchy stress tensor σ and the consistent elastic stiffness tensor C are given by

$$\sigma = (1-d)^2 \frac{d\Psi_e^+}{d\epsilon} + \frac{d\Psi_e^-}{d\epsilon}, \quad (5)$$

$$C = (1-d)^2 \frac{d^2 \Psi_e^+}{d\epsilon^2} + \frac{d^2 \Psi_e^-}{d\epsilon^2}, \quad (6)$$

where $\epsilon = \frac{1}{2} [\nabla \mathbf{u} + (\nabla \mathbf{u})^T]$ is the linearized strain tensor. Now, using the above relations, the total energy in the body is

$$\Pi(\mathbf{u}, d) = \int_{\Omega} [(1-d)^2 \Psi_e^+ + \Psi_e^- + \frac{3G_c}{8l} (d + l^2 \nabla d \cdot \nabla d)] d\Omega. \quad (7)$$

Further, to impose irreversibility of the crack evolution in computer simulations, a history field \mathcal{H} is used in place of Ψ_e^+ , such that \mathcal{H} is the maximum positive strain energy density experienced (Miehe et al., 2010b), i.e.,

$$\mathcal{H}(\mathbf{u}, t) = \max_{\tau \in [0, t]} \{ \Psi_e^+(\mathbf{u}, \tau) \}, \quad (8)$$

where t denotes time. The history field (8) ensures that it is the highest strain energy density experienced in the material during the loading history that determines the present damage state, i.e. the material cannot heal. Stresses are however reversible, and are always evaluated according to (5).

The first variation of (7) should be zero according to the principle of minimization of potential energy. The Euler–Lagrange equations of (7) with respect to the displacement and damage fields are,

$$\begin{cases} \nabla \cdot \sigma = 0 \\ (1-d)\mathcal{H} - \frac{3G_c}{16l} - \frac{3G_c l}{8} \nabla^2 d = 0. \end{cases} \quad (9)$$

2.1. Spectral decomposition

The spectral decomposition was introduced by Miehe et al. (2010b), who decomposed Ψ_e using the tensile deformation states. In terms of the Lamé parameters λ and μ , the strain energy density in an isotropic linear elastic material can be written as $\Psi_e = \frac{1}{2} \lambda (\text{tr } \epsilon)^2 + \mu \text{tr } (\epsilon^2)$. The term including λ is only related to volumetric deformation, whereas the term associated with μ includes both volume and shape changes. Since $\text{tr } \epsilon$ and $\text{tr } (\epsilon^2)$ are invariants of the strain tensor, they do not change with any rotation of the coordinate system, which allows an elegant split of the strain energy density into positive and negative parts using the principal strains. The first step is to express Ψ_e in terms of the principal strains ϵ_1, ϵ_2 and ϵ_3 as $\Psi_e = \frac{1}{2} \lambda (\epsilon_{11} + \epsilon_{22} + \epsilon_{33})^2 + \mu (\epsilon_1^2 + \epsilon_2^2 + \epsilon_3^2)$. The strain energy density is then separated into positive and negative parts using the strictly positive and negative terms, $\Psi_e^{\pm} = \frac{1}{2} \lambda \langle \epsilon_{11} + \epsilon_{22} + \epsilon_{33} \rangle_{\pm}^2 + \mu \langle \epsilon_1 \rangle_{\pm}^2 + \mu \langle \epsilon_2 \rangle_{\pm}^2 + \mu \langle \epsilon_3 \rangle_{\pm}^2$, where $\langle \cdot \rangle_{+}$ and $\langle \cdot \rangle_{-}$ selects the positive and negative parts of their argument, i.e. $\langle x \rangle_{+} = x$, if $x \geq 0$; 0 if $x < 0$, and $\langle x \rangle_{-} = x$, if $x \leq 0$; 0 if $x > 0$.

2.2. Hydrostatic–deviatoric decomposition

The hydrostatic–deviatoric decomposition was introduced by Amor et al. (2009), who argue that crack growth is driven by shear and tensile bulk deformation, which from a theoretical point of view is well justified. For isotropic linear elastic materials, the bulk deformation is one of the fundamental eigenmodes of the stiffness matrix and the corresponding eigenvalue is the bulk modulus. This eigenmode is, in fact, the spherical part of the strain while the other eigenmodes are related to shear deformation and the shear modulus. The strain tensor is decomposed into a hydrostatic and a deviatoric part as $\epsilon = \epsilon_K \mathbf{1} + \mathbf{e}$ where $\mathbf{1}$ is the second-order identity tensor, \mathbf{e} is the deviatoric strain tensor and ϵ_K is the hydrostatic strain $\epsilon_K = \text{tr } \epsilon / n$ (n is the number of spatial dimensions). Using the bulk modulus $K = \lambda + 2\mu/n$, the strain energy density can then be written $\Psi_e = \frac{1}{2}K (\text{tr } \epsilon)^2 + \mu \text{tr } (\mathbf{e}^2)$ and split into a negative part $\Psi_e^- = \frac{1}{2}K \langle \text{tr } \epsilon \rangle_-^2$ and a crack-driving positive part $\Psi_e^+ = \frac{1}{2}K \langle \text{tr } \epsilon \rangle_+^2 + \mu \text{tr } (\mathbf{e}^2)$.

2.3. Hydrostatic–spectral–deviatoric decomposition

Recall the hydrostatic–deviatoric decomposition,

$$\Psi_e^+ = \frac{1}{2}K \langle \text{tr } \epsilon \rangle_+^2 + \mu \text{tr } (\mathbf{e}^2), \quad \Psi_e^- = \frac{1}{2}K \langle \text{tr } \epsilon \rangle_-^2. \quad (10)$$

A first step is to express the deviatoric part $\Psi_{\text{dev}} = \mu \text{tr } (\mathbf{e}^2)$ in terms of the principal strains, i.e.

$$\begin{aligned} \Psi_{\text{dev}} &= \mu [e_1^2 + e_2^2 + e_3^2] - \mu \frac{1}{n} [e_1 + e_2 + e_3]^2 \\ &= \mu \frac{n-1}{n} [e_1^2 + e_2^2 + e_3^2] - \mu \frac{2}{n} [e_1 e_2 + e_1 e_3 + e_2 e_3]. \end{aligned} \quad (11)$$

We separate (11) so that $\Psi_{\text{dev}} = \Psi_{\text{dev}}^+ + \Psi_{\text{dev}}^-$ using the spectral decomposition of the strain tensor into positive and negative parts (where cross-terms of the form $\langle \epsilon_i \rangle_+ \langle \epsilon_i \rangle_-$ naturally vanish)

$$\begin{aligned} \Psi_{\text{dev}}^+ &= \mu \frac{n-1}{n} [\langle \epsilon_1 \rangle_+^2 + \langle \epsilon_2 \rangle_+^2 + \langle \epsilon_3 \rangle_+^2] - \mu \frac{2}{n} [\langle \epsilon_1 \rangle_+ \langle \epsilon_2 \rangle_- + \langle \epsilon_2 \rangle_+ \langle \epsilon_1 \rangle_- \\ &\quad + \langle \epsilon_1 \rangle_+ \langle \epsilon_3 \rangle_- + \langle \epsilon_3 \rangle_+ \langle \epsilon_1 \rangle_- + \langle \epsilon_2 \rangle_+ \langle \epsilon_3 \rangle_- + \langle \epsilon_3 \rangle_+ \langle \epsilon_2 \rangle_-], \end{aligned} \quad (12)$$

$$\Psi_{\text{dev}}^- = \mu \frac{n-1}{n} [\langle \epsilon_1 \rangle_-^2 + \langle \epsilon_2 \rangle_-^2 + \langle \epsilon_3 \rangle_-^2]. \quad (13)$$

It is noticed that both Ψ_{dev}^+ and Ψ_{dev}^- consist solely of invariants of the strain tensor ϵ and are thus independent of any rotation of the coordinate system. Using (10)–(13), a unified hydrostatic–spectral–deviatoric split can now be formulated as

$$\begin{aligned} \Psi_e^+ &= \frac{1}{2}K \langle \text{tr } \epsilon \rangle_+^2 + \Psi_{\text{dev}}^+ + \phi \Psi_{\text{dev}}^-, \\ \Psi_e^- &= \frac{1}{2}K \langle \text{tr } \epsilon \rangle_-^2 + (1 - \phi) \Psi_{\text{dev}}^-, \end{aligned} \quad (14)$$

where ϕ is a variable which can take the value 0 or 1. When $\phi = 1$ the original hydrostatic–deviatoric split is recovered (10); when $\phi = 0$, compressive strains (13) contribute to the negative part and do not take part in the crack growth process. It is noticed that all positive strains and cross-terms (12) are in the positive part of the deviatoric energy density and always contribute in the crack-driving process.

How to select ϕ ? There are several criteria suggested in the literature to judge whether or not fracture occurs under compressive loads. The most commonly used is probably the classic Mohr failure criterion, cf. Labuz and Zang (2012), which is a set of linear equations in principal strain (or stress) space describing the conditions for which an isotropic material will fail. Advantages of the Mohr failure criterion are its mathematical simplicity, clear physical meaning of the material parameters, and general level of acceptance in the scientific community. Without going into details, a fracture surface f is defined as (sorting $\epsilon_1 \geq \epsilon_2 \geq \epsilon_3$)

$$f = \frac{\lambda + \mu}{\mu} \frac{\epsilon_1 + \epsilon_3}{\epsilon_1 - \epsilon_3} \sin \theta - \frac{c}{\mu(\epsilon_1 - \epsilon_3)} \cos \theta + 1, \quad (15)$$

where c is an inherent cohesive stress and θ is an angle of internal friction, Fig. 2. One may notice that the cohesive stress scales to G_c , l , and μ as $c \sim \sqrt{\mu G_c / l}$.

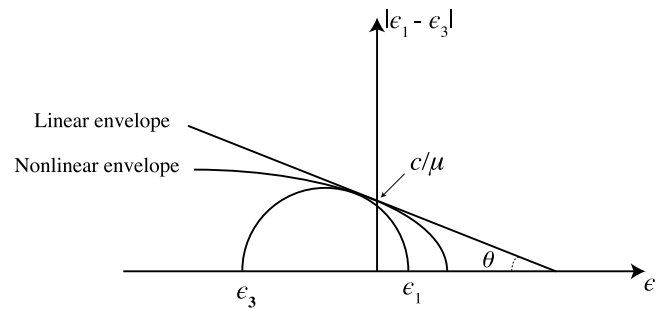


Fig. 2. Mohr diagram and failure envelopes.

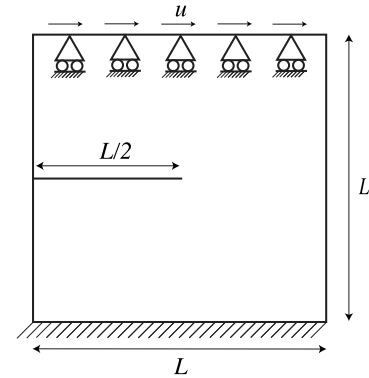


Fig. 3. The shear test model.

The Mohr criterion allows a curved shape of the failure envelope, and this nonlinear behavior is exhibited by many rock types, Jaeger et al. (2009), however, for simplicity we stick to the linear envelope (15) here. Using (15), crack growth take place when $f \geq 0$, wherefore ϕ in (14) is readily given by the present strain state according to

$$\phi = 1 \text{ if } f \geq 0, \text{ else } \phi = 0. \quad (16)$$

3. Models

The validity of the hydrostatic–spectral–deviatoric strain energy density decomposition (14) is demonstrated using three two-dimensional models with simple loading scenarios as reference.

3.1. Single edge notch shear test

Consider the canonical example of global remote shear loading, Fig. 3: a two-dimensional quadratic specimen with side length $L = 1$ mm, its lower horizontal boundary fully clamped and its upper horizontal boundary displaced in the horizontal direction while constrained in the vertical direction. The two vertical boundaries are held stress free. A horizontal edge crack of length $L/2$ is positioned at the mid-height of the specimen. The material parameters are: Young's modulus $E = 210$ GPa, Poisson's ratio $\nu = 0.3$ and the fracture toughness $G_c = 2700$ N/m. The two additional material parameters required in (14) are: the cohesive strength $c = 10.5$ GPa and the internal friction angle $\theta = \pi/6$. A uniform mesh with an element edge length of $h = 7.5$ μm is used, and the regularization length is set to $l = 2h$.

3.2. Flattened Brazilian disk test

Consider a flattened Brazilian disk test, Fig. 4, designed for estimating both the tensile strength and fracture toughness of rocks, cf. Yu et al. (2021). The radius of the compressed cylinder is $R = 67.5$ mm, the load angle $\alpha = 30^\circ$ while the material parameters are: Young's

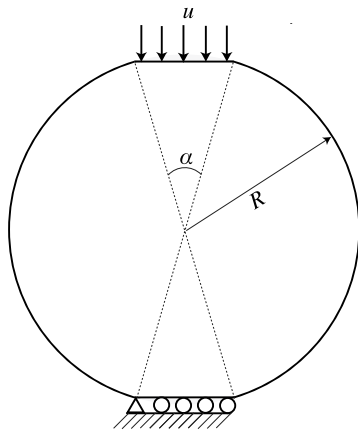


Fig. 4. Flattened Brazilian disk model.

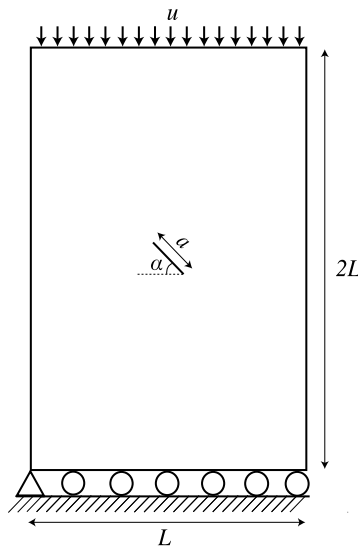


Fig. 5. Specimen with an inclined notch.

modulus $E = 3.85$ GPa, Poisson's ratio $\nu = 0.2$. The fracture toughness, cohesive strength, and the internal friction angle are $G_c = 700$ N/m, $c = 200$ MPa, and $\theta = \pi/6$, respectively. The lower horizontal boundary of the specimen is constrained while the upper horizontal boundary is subject to vertical displacements. The other boundaries are held stress free. A non-uniform mesh with a maximum element edge length of $h = 1$ mm is used, (the mesh is denser at the center of the body) and the regularization length is set to $l = 2h$.

3.3. Inclined notch

Consider uniaxial compressive loading of a brittle rock-like material. The specimen has height $2L$, width L ($L = 50$ mm), and a centered straight internal notch with length $a = 12$ mm, inclined $\alpha = 45^\circ$, Nguyen (2011). The lower horizontal boundary of the specimen is constrained while the upper horizontal boundary is subject to vertical displacements, Fig. 5. The vertical boundaries are held stress free. The material parameters are: Poisson's ratio $\nu = 0.18$ and a Young's modulus $E = 5$ GPa (which is reported being in the upper range of the stiffness measured during the experiments, Nguyen, 2011). The fracture toughness G_c , cohesive strength c and internal friction angle θ are 23 N/m, 62.8 MPa, and $\pi/6$, respectively. The mesh is nearly uniform with a maximum edge length $h = 106$ μ m and a regularization length $l = 2h$ is used.

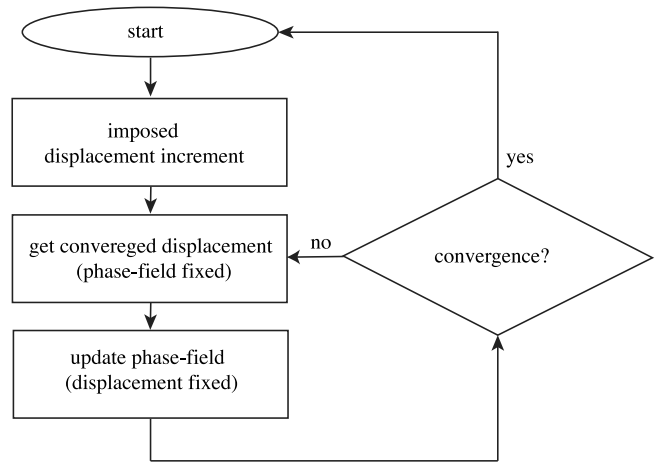


Fig. 6. Flowchart of the staggered scheme used in the quasi-static simulations.

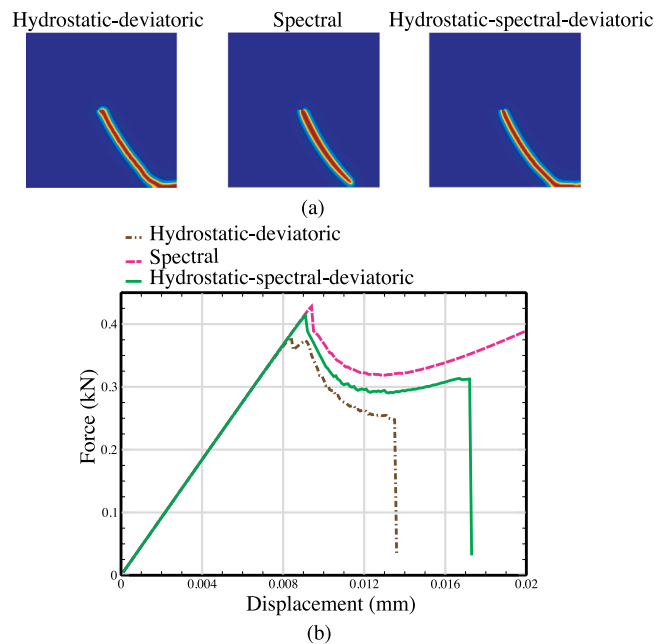


Fig. 7. Single edge notch shear test: crack paths (a) and global force–displacement curves (b).

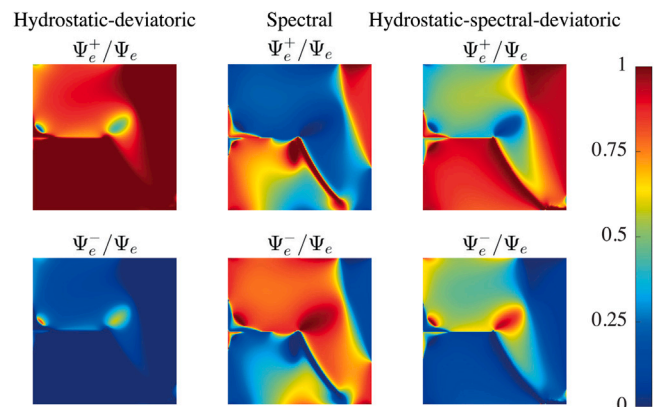


Fig. 8. Distributions of normalized positive and negative strain energy densities in the last load step for the shear test.

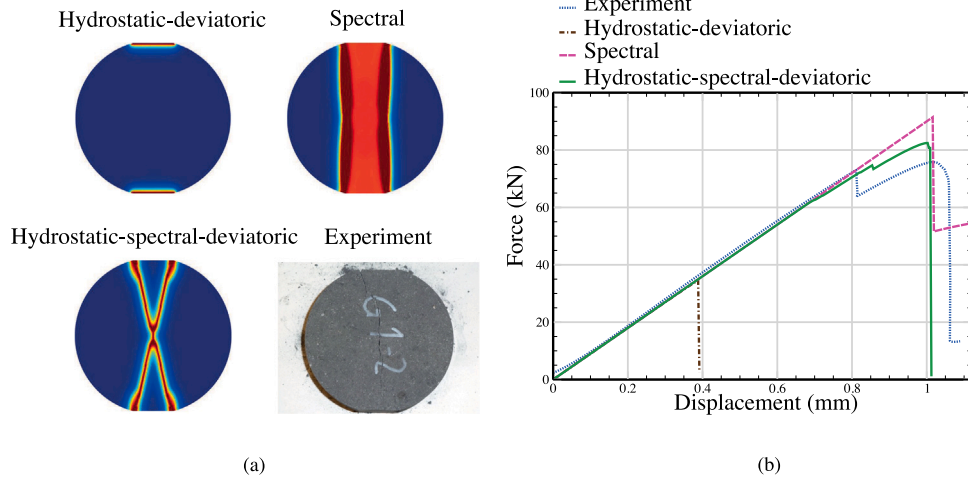


Fig. 9. Flattened Brazilian disk test: crack paths (a) and global force–displacement curves (b).
Source: Experimental results are taken from Yu et al. (2021).

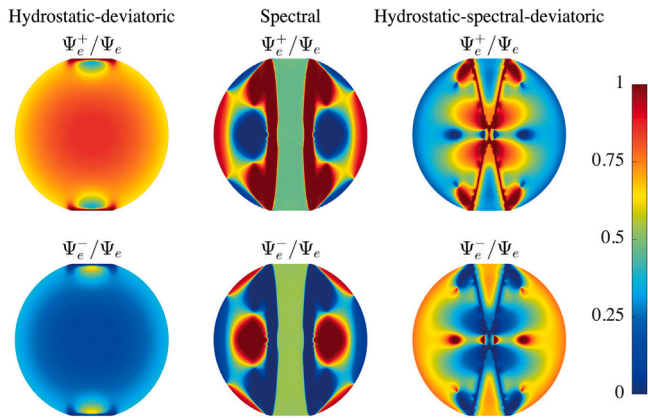


Fig. 10. Distributions of normalized positive and negative strain energy densities in the last load step for the Brazilian test.

4. Results and discussion

All the quasi-static simulations are solved using a staggered Newton–Raphson scheme. For each load step t , the displacement field \mathbf{u} and damage field d are solved and updated sequentially in an iteration process until tolerances of the incremental change is sufficiently small and force equilibrium prevails. For the displacement problem, a classical out-of-balance force criterion (Bathe, 1996) is used to determine when convergence is achieved (tolerance is 10^{-8}). For the damage problem, convergence is obtained when the maximum of the incremental nodal damage field (absolute value) is less than 10^{-3} . A flowchart of the staggered scheme adopted is shown in Fig. 6.

Discretization is done by interpolating the displacement and phase-field variables with standard finite element shape functions. Typical discretization examples can be found in e.g. Espadas-Escalante et al. (2019). All equations are solved using well-established finite element algorithms implemented in a Matlab (MATLAB, 2021) code. Standard bi-linear 4-node isoparametric elements assuming plane strain conditions are used for all computations, in which the Lamé coefficients are $\mu = E/[2(1 + \nu)]$ and $\lambda = E\nu/[(1 + \nu)(1 - 2\nu)]$. Small deformations are assumed to prevail and the displacement load is applied incrementally in small steps. The imposed incremental displacements for the shear test, the Brazilian test, and the inclined notch test are $0.1 \mu\text{m}$, $3.4 \mu\text{m}$ and $0.6 \mu\text{m}$, respectively.

In all simulations, the computed damage fields were always in the range ($0 \leq d \leq 1$), thus, any problems related to damage > 1 that has been observed in e.g. Wu et al. (2020) was not encountered.

4.1. Single edge notch shear test

Simulations were carried out using the three decomposition strategies elaborated above. The resulting global force–displacement relations as well as the final cracks are shown in Fig. 7. Distributions of normalized positive and negative strain energy densities for the last load step are presented in Fig. 8. The hydrostatic–deviatoric decomposition results in global stiffness loss, in strong contrast to the spectral decomposition, which never results in complete stiffness loss even though the crack reaches the lower edge. This non-physical behavior of the spectral decomposition is explained by the second part of Ψ_e^- , i.e. $\mu[\langle \epsilon_1 \rangle_-^2 + \langle \epsilon_2 \rangle_-^2 + \langle \epsilon_3 \rangle_-^2]$. In a material point, predominantly shear loading (as in the lower part of the specimen, between the tip and the right vertical edge) results in both a positive principal strain $\epsilon_1 > 0$ and a negative principal strain $\epsilon_3 < 0$. Since $\Psi_e^- > 0$ (Fig. 8), and because the material stiffness tensor $\mathbf{C} = (1 - d)^2 d^2 \Psi_e^+ / de^2 + d^2 \Psi_e^- / de^2$, one realize that stiffness never will be lost in shear dominated scenarios, even if a crack is fully developed ($d = 1$). This is observed in that the remaining global stiffness is about 50% of the body’s initial stiffness. In sharp contrast, the hydrostatic–deviatoric decomposition results in complete stiffness loss as long as the hydrostatic strain ≥ 0 . Similarly, the developed hydrostatic–spectral–deviatoric decomposition, enhanced with a Mohr failure criterion, also results in complete global stiffness loss when the crack reaches the boundary. The developed decomposition produces results for this load case that are very close to the original hydrostatic–deviatoric decomposition. This similarity can be seen in the distributions of positive and negative strain energy densities in the cracked regions for each of these methods as well (Fig. 8).

4.2. Flattened Brazilian disk test

Simulations were carried out using the three decomposition strategies. The resulting global force–displacement relations as well as the final cracks are shown in Fig. 9. Experimental results from literature (Yu et al., 2021) are shown as well. The distributions of normalized positive and negative strain energy densities for the last load step are shown in Fig. 10. The hydrostatic–deviatoric decomposition results in almost instant global stiffness loss: shear cracks are developed slightly below the contact surfaces leading to totally deteriorated material, which in turn lead to volume expansion whereupon the negative part of the decomposition, Ψ_e^- , vanishes, which can also be judged from Fig. 10. Since $d = 1$ below the contact and $\mathbf{C} = (1 - d)^2 d^2 \Psi_e^+ / de^2 + d^2 \Psi_e^- / de^2$, the local material stiffness tensor at the contacts vanishes, i.e. $\mathbf{C} \rightarrow 0$, as is observed in Fig. 9. The behavior of the spectral decomposition is entirely different. Also in this example, the spectral

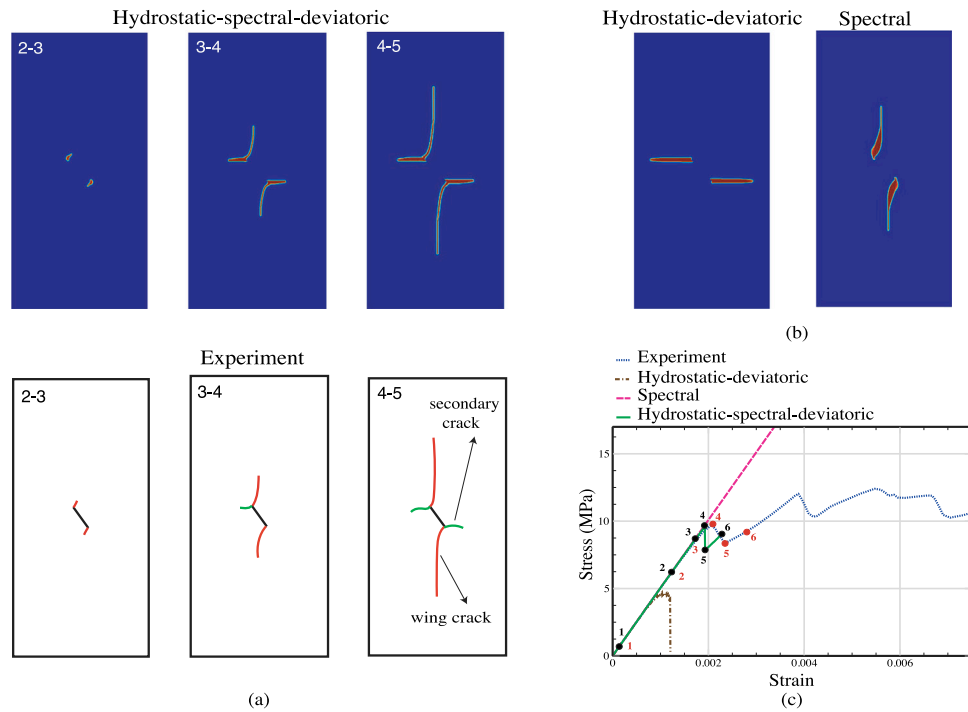


Fig. 11. Inclined notch. Crack paths for the experiment and the developed decomposition model (a), for the hydrostatic–deviatoric and the spectral decomposition models (b). Global stress–strain curves (c).

Source: Experimental results are redrawn from Nguyen (2011).

decomposition never results in complete stiffness loss even though two vertical cracks extend between the top and bottom, separating the body into three isolated parts, Fig. 9. Similar to the discussion of the single edge notch test, the loading results in both a positive principal strain $\epsilon_1 > 0$ and a negative principal strain $\epsilon_3 < 0$. Since $\Psi_e^- > 0$, stiffness will never be lost. This is manifested in that the global stiffness of the fractured body is roughly half of its initial stiffness (as can also be interpreted in Fig. 10). In strong contrast to both the hydrostatic–deviatoric decomposition and the spectral decomposition, the developed decomposition produces fractures that extends diagonally over the cross-section, resulting in complete stiffness loss, Figs. 9 and 10. It is noted that only one diagonal crack was observed in the experiment, probably due to the heterogeneity of a real-life specimen, while two cracks were produced in the simulation due to perfect symmetry and the assumption of a homogeneous material. Nevertheless, a similarity in crack patterns can be seen between experiment and simulation. Further, a fairly good agreement is observed in the global load–displacement curves in Fig. 9. Not only the developed hydrostatic–spectral–deviatoric decomposition results in complete stiffness loss, it also produces a kink in the global loading curve, which is linked to onsets of crack growth, and is also observed in the experiment.

4.3. Inclined notch

Simulations were carried out using the three decomposition strategies. The resulting stress–strain relations as well as the final cracks are shown in Fig. 11. Experimental results from literature (Nguyen, 2011) are shown as well. In Fig. 12 are the distributions of normalized positive and negative strain energy densities for the last load step presented. Using the hydrostatic–deviatoric decomposition, only the secondary cracks are obtained while when using the spectral decomposition, only the wing cracks are obtained, Fig. 11b. Similar to the two load scenarios discussed above, the hydrostatic–deviatoric decomposition results in an almost immediate global stiffness loss while the spectral decomposition never results in global stiffness loss, Fig. 11c. However, the hydrostatic–spectral–deviatoric decomposition enhanced with Mohr

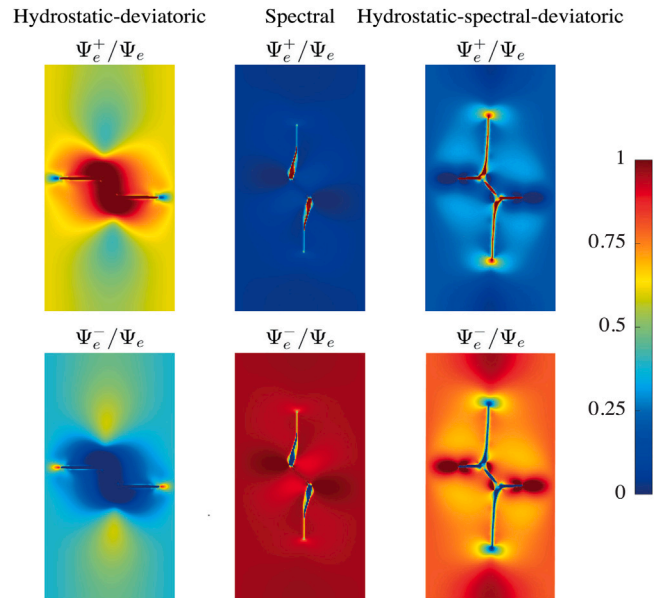


Fig. 12. Distributions of normalized positive and negative strain energy densities in the last load step for the inclined notch test.

failure criterion, is capable of capturing both type of cracks, i.e., both wing cracks and secondary cracks. Fig. 12 provides an indication of all these observations. The simulations were terminated either when global stiffness loss was achieved or when a crack had grown sufficiently close to a boundary (about half the distance between the initial tip and boundary). In the simulation using the hydrostatic–spectral–deviatoric decomposition, Fig. 11a, wing cracks nucleate (at marker 3) and grow stably in the vertical direction until peak load (marker 4), followed by unstable secondary cracks, which emerge horizontally on the opposite side from the wing cracks, from the tips of the initial notch. The propagation of secondary cracks then slows down (marker 5). The crack

evolution is compared to the experimental sample, and they are in good agreement, at least up to marker 6. It should be noted that this set of experimental data (Nguyen, 2011) was used by Spetz et al. (2021) to verify a modified decomposition in a phase-field fracture model. Very good agreement with the experiment was obtained in their work regarding the crack pattern, and markers 3 and 4 on the loading curve were well captured. However, their model failed to capture marker 5 (and beyond) and resulted in complete stiffness loss. Spetz et al. (2021) argued that the reason for the global stiffness loss after marker 5 is related to lack of contact formulations of the crack lips of the initial inclined notch. However, one observes that contact formulations are not included in our model, still marker 5 and marker 6 are captured.

Finally, it should be said that the enhanced decomposition (14) can quite easily be further extended by e.g. including separate fracture toughnesses for opening and shearing modes, similar to e.g. Zhang et al. (2017) or Spetz et al. (2021), following the original idea of Shen and Stephansson (1994). However, this is beyond the scope for this study.

5. Conclusion

In phase-field fracture models are decompositions (or splits) of the strain energy density vital to avoid interpenetration of crack surfaces and to select physically trustworthy crack paths. The most popular decomposition strategies use either a spectral decomposition or a hydrostatic–deviatoric decomposition. It is illustrated that these popular decompositions can have significant disadvantages; the most important is that none of them can handle mixed-mode load scenarios in compression.

To circumvent these problems, a generalized decomposition method is derived that unifies some features of the hydrostatic–deviatoric and spectral decompositions enhanced with the classical Mohr–Coulomb failure criterion. The enhanced decomposition consists solely of invariants of the strain tensor and is thus independent of any rotation of the coordinate system. Compared to the two popular decompositions, the enhanced decomposition requires two additional material parameters, both connected to Mohr failure criterion: a cohesive stress (strain) parameter and an internal friction parameter.

The derived decomposition scheme has the potential to judge whether or not a compressive deformation field will assist in the crack driving process in brittle materials. The decomposition is scrutinized in numerical models and biaxially loaded crack experiments in global compression. Simulations using the decomposition scheme capture the experiments in a remarkable way: complex crack patterns are reproduced as well as critical loads. The enhanced decomposition strategy hence provides deeper mechanistic insight into fracture processes in brittle materials subject to mixed-mode loads. Finally, the formulation can easily be further extended by e.g. including separate fracture toughnesses for opening and shearing modes, following Shen and Stephansson (1994).

Declaration of competing interest

The authors declare that they have no known competing financial interests or personal relationships that could have appeared to influence the work reported in this paper.

Data availability

The data that has been used is confidential.

Acknowledgment

The authors would like to acknowledge the Swedish Research Council [grant no. 2016-04608] for the financial support.

References

- Ambati, M., Gerasimov, T., De Lorenzis, L., 2015. A review on phase-field models of brittle fracture and a new fast hybrid formulation. *Comput. Mech.* 55 (2), 383–405.
- Amor, H., Marigo, J.-J., Maurini, C., 2009. Regularized formulation of the variational brittle fracture with unilateral contact: Numerical experiments. *J. Mech. Phys. Solid* 57 (8), 1209–1229.
- Areias, P., Msekhi, M., Rabczuk, T., 2016. Damage and fracture algorithm using the screened Poisson equation and local remeshing. *Eng. Fract. Mech.* 158, 116–143.
- Armero, F., Linder, C., 2009. Numerical simulation of dynamic fracture using finite elements with embedded discontinuities. *Int. J. Fract.* 160 (2), 119–141.
- Bathe, K.-J., 1996. *Finite Element Procedures*. Prentice-Hall.
- Borden, M.J., Verhoosel, C.V., Scott, M.A., Hughes, T.J., Landis, C.M., 2012. A phase-field description of dynamic brittle fracture. *Comput. Methods Appl. Mech. Eng.* 217, 77–95.
- Bourdin, B., Francfort, G.A., Marigo, J.-J., 2000. Numerical experiments in revisited brittle fracture. *J. Mech. Phys. Solid* 48 (4), 797–826.
- Braides, A., 1998. *Approximation of Free-Discontinuity Problems*. (1994), Springer.
- Cajuhí, T., Sanavia, L., De Lorenzis, L., 2018. Phase-field modeling of fracture in variably saturated porous media. *Comput. Mech.* 61 (3), 299–318.
- Carlsson, J., Isaksson, P., 2018. Dynamic crack propagation in wood fibre composites analysed by high speed photography and a dynamic phase field model. *Int. J. Solids Struct.* 144, 78–85.
- Carlsson, J., Isaksson, P., 2019. Crack dynamics and crack tip shielding in a material containing pores analysed by a phase field method. *Eng. Fract. Mech.* 206, 526–540.
- Espadas-Escalante, J.J., van Dijk, N.P., Isaksson, P., 2019. A phase-field model for strength and fracture analyses of fiber-reinforced composites. *Compos. Sci. Technol.* 174, 58–67.
- Espadas-Escalante, J.J., Isaksson, P., 2019. Mesoscale analysis of the transverse cracking kinetics in woven composite laminates using a phase-field fracture theory. *Eng. Fract. Mech.* 216, 106523.
- Francfort, G.A., Marigo, J.-J., 1998. Revisiting brittle fracture as an energy minimization problem. *J. Mech. Phys. Solid* 46 (8), 1319–1342.
- Hofacker, M., Miehe, C., 2012. Continuum phase field modeling of dynamic fracture: variational principles and staggered FE implementation. *Int. J. Fract.* 178 (1), 113–129.
- Jaeger, J.C., Cook, N.G., Zimmerman, R., 2009. *Fundamentals of Rock Mechanics*. John Wiley & Sons.
- Kuhn, C., Müller, R., 2016. A discussion of fracture mechanisms in heterogeneous materials by means of configurational forces in a phase field fracture model. *Comput. Methods Appl. Mech. Eng.* 312, 95–116.
- Labuz, J.F., Zang, A., 2012. Mohr–Coulomb failure criterion. *Rock Mech. Rock Eng.* 45 (6), 975–979.
- Larsen, C.J., Ortner, C., Süli, E., 2010. Existence of solutions to a regularized model of dynamic fracture. *Math. Models Methods Appl. Sci.* 20 (07), 1021–1048.
- MATLAB, 2021. R2021b. The MathWorks Inc., Natick, Massachusetts.
- Miehe, C., Hofacker, M., Welschinger, F., 2010a. A phase field model for rate-independent crack propagation: Robust algorithmic implementation based on operator splits. *Comput. Methods Appl. Mech. Eng.* 199 (45–48), 2765–2778.
- Miehe, C., Welschinger, F., Hofacker, M., 2010b. Thermodynamically consistent phase-field models of fracture: Variational principles and multi-field FE implementations. *Internat. J. Numer. Methods Engrg.* 83 (10), 1273–1311.
- Moës, N., Belytschko, T., 2002. Extended finite element method for cohesive crack growth. *Eng. Fract. Mech.* 69 (7), 813–833.
- Nguyen, T.L., 2011. *Endommagement localisé dans les roches tendres. Expérimentation par mesure de champs* (Ph.D. thesis). Grenoble.
- Peerlings, R., Borst, R., Brekelmans, W., Vree, J., Spee, I., 1996. Some observations on localization in non-local and gradient damage models. *Eur. J. Mech. A Solids* 15 (6), 937–953.
- Pham, K., Amor, H., Marigo, J.-J., Maurini, C., 2011. Gradient damage models and their use to approximate brittle fracture. *Int. J. Damage Mech.* 20 (4), 618–652.
- Pham, K., Ravi-Chandar, K., Landis, C., 2017. Experimental validation of a phase-field model for fracture. *Int. J. Fract.* 205 (1), 83–101.
- Santillán, D., Mosquera, J.C., Cueto-Felgueroso, L., 2017. Phase-field model for brittle fracture. Validation with experimental results and extension to dam engineering problems. *Eng. Fract. Mech.* 178, 109–125.
- Schlüter, A., Kuhn, C., Müller, R., Gross, D., 2016. An investigation of intersonic fracture using a phase field model. *Arch. Appl. Mech.* 86 (1), 321–333.
- Shen, B., Stephansson, O., 1994. Modification of the G-criterion for crack propagation subjected to compression. *Eng. Fract. Mech.* 177–189.
- Spetz, A., Denzer, R., Tudisco, E., Dahlblom, O., 2020. Phase-field fracture modelling of crack nucleation and propagation in porous rock. *Int. J. Fract.* 224 (1), 31–46.
- Spetz, A., Denzer, R., Tudisco, E., Dahlblom, O., 2021. A modified phase-field fracture model for simulation of mixed mode brittle fractures and compressive cracks in porous rock. *Rock Mech. Rock Eng.* 54 (10), 5375–5388.
- Wu, J.-Y., Nguyen, V.P., Nguyen, C.T., Sutula, D., Sinaia, S., Bordas, S.P., 2020. Phase-field modeling of fracture. *Adv. Appl. Mech.* 53, 1–183.
- Yu, H., Andersen, D.H., He, J., Zhang, Z., 2021. Is it possible to measure the tensile strength and fracture toughness simultaneously using flattened Brazilian disk? *Eng. Fract. Mech.* 247, 107633.
- Zhang, X., Sloan, S.W., Vignes, C., Sheng, D., 2017. A modification of the phase-field model for mixed mode crack propagation in rock-like materials. *Comput. Methods Appl. Mech. Eng.* 322, 123–136.